SCIENTIFIC REPORTS
nature research

OPEN

Annealing Effect of Glancing Angle Electron Beam Deposited TiO_2/In_2O_3 Nanowires Array on Surface Wettability

Pheiroijam Pooja & Chinnamuthu P. ✉

TiO_2/In_2O_3 nanowire (NW) array are prepared using catalyst free glancing angle deposition technique. The wettability of TiO_2/In_2O_3 NW surface are tuned and controlled by the annealing treatment without altering the surface with additional chemical coating. The phase change, surface roughness, change in static and dynamic contact angles due to the heat treatment are studied. Moreover, the surface properties such as frictional force and work of adhesion are calculated for all the samples. The samples annealed at 600 °C shows nearly superhydrophilic with static water contact angle of 12°, frictional force of 85.00748 µN and work of adhesion of 142.3721 mN/m. The surface of TiO_2/In_2O_3 NW is controlled to attain desired water contact angles and sliding angles, which is paramount for designing practical application in self-cleaning, electronic and biomedical fields.

Surfaces with superhydrophilic wetting nature have been used in numerous applications such as anti-fogging, self-cleaning coatings and tissue reconstruction[1–5]. Controlling the wettability of surface is desirable in various technical applications. In recent years, efforts have been made to improve the hydrophilicity of thin films. There are works on improvement of hydrophilicity using UV illumination of metaloxide films such as TiO_2, SnO_2 and ZnO either doping by metal or non-metal[6,7]. However, there are limitations in the application of these metal oxides for use as a reliable superhydrophilic coating and thus need to be checked. For practical application, surface of the film cannot be illuminated with UV light all the time and there is need of long lasting hydrophilicity in absence of UV illumination for anti-fogging surfaces, specifically in outdoor applications. We have reported on designing vertical stacked coaxial TiO_2-In_2O_3 heterostructure nanowire (NW), which studies on photoinduced hydrophilicity after UV-illumination[8]. There are also reports on hydrophobic to hydrophilic conversion using surface derivatization, chemical grafting, wet chemical reactions and also modifying hydrophobic cross linked high internal phase emulsion polymer (polyHIPE) using styrene[9–11]. Problems associated with these techniques are difficulties in implementation, high cost, polymer degradation possibility and scale up issues for large industrial production.

There is no report on study of tuning the wettability of coaxial TiO_2-In_2O_3 NW from hydrophobic to hydrophilic through simple heat treatment. Moreover, before TiO_2/In_2O_3 NWs are utilized successfully, annealing is necessary to improve the NWs crystallinity. During elevated annealing temperature, the solid-state sintering of TiO_2 nanostructure subsequently causes structure breakdown. Such results are more noticeable when there is enhanced mass transport and bond breaking during phase transformation from anatase to rutile[12,13]. In case of In_2O_3, at elevated annealing temperature the grain stops growing or exhibits amorphous nature[14,15]. Therefore, it is mandatory to elucidate the dependence of thermal stability of desired crystalline phase and nanostructure itself on the annealing temperature, especially for high temperature applications. Detailed study on the structural transformations due to various annealing effects of coaxial TiO_2-In_2O_3 NW structure has not been investigated elsewhere which studies about the phase changes, surface states and surface wettability stability. Further, there is shortage in growth techniques of perpendicularly aligned coaxial NW. Few techniques have been reported for the synthesis of coaxial heterostructure nanowires namely wet chemical synthesis, pulsed laser ablation along with chemical vapor deposition (CVD) and metal organic chemical vapor deposition (MOCVD)[16–18]. In all these methods, growth controlling is difficult and is catalyst assisted. Glancing angle deposition (GLAD) technique

Department of Electronics and Communication Engineering, National Institute of Technology Nagaland, Chumukedima, Dimapur, 797103, India. ✉e-mail: chinnamuthu@nitnagaland.ac.in

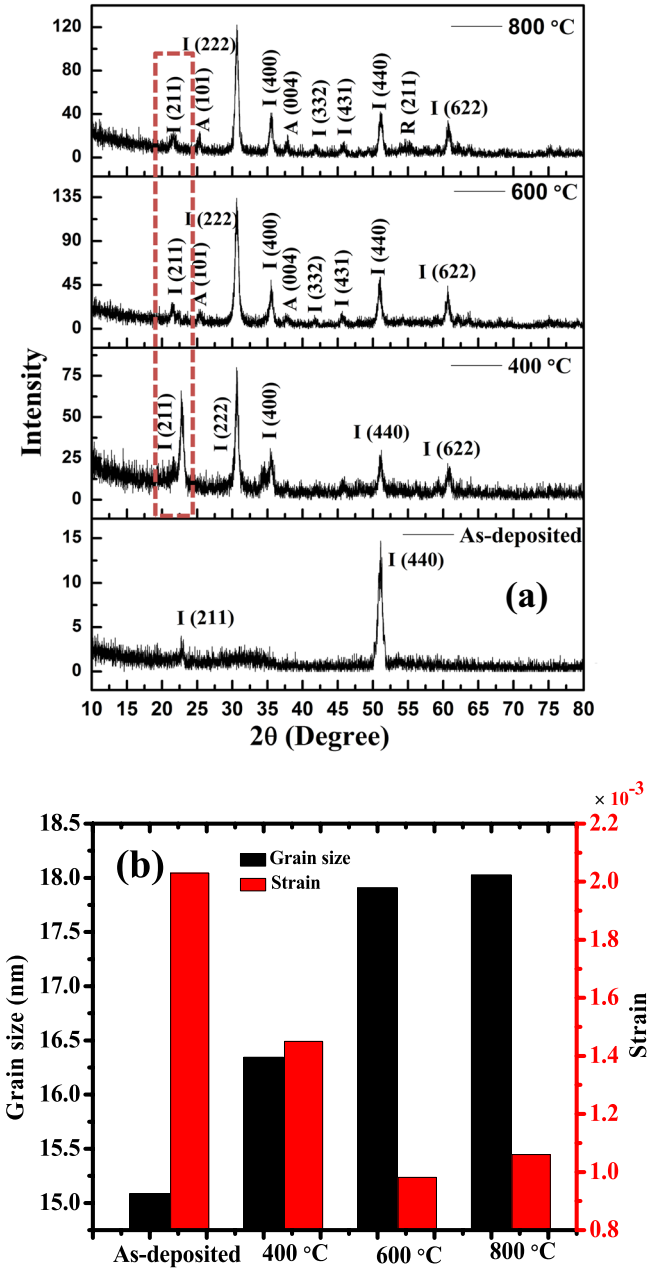

Figure 1. TiO_2-In_2O_3 NWs as-deposited and annealed samples (**a**) XRD and (**b**) size-strain plot.

is catalytic free and an efficient way for controlling the growth parameters such as morphology, porosity and thickness[19].

In this paper, 1D TiO_2-In_2O_3 heterostructure NW has been synthesized using GLAD technique. The structure properties for annealed samples are studied. Attempt has been made to compare the phase transition and textural changes under thermal treatment of 1D TiO_2-In_2O_3 NW. The surface properties are also studied to evaluate the annealing effects on samples for understanding its possible applications.

Results and Discussions

Figure 1(a) shows the XRD analysis of TiO_2-In_2O_3 NWs deposited on Si (100) substrates as a function of temperature (400–800 °C) and Fig. 1(b) shows the size-strain graph versus as deposited and annealed samples calculated from the Eq. (1)[20] given below:

$$\beta \cos\theta = \frac{k\lambda}{D} + 4 \in \sin\theta \tag{1}$$

Where D stands for crystallite size, λ stands for wavelength of incident light, k is constant (=0.9), θ is bragg angle, β is the full width half maximum of peaks.

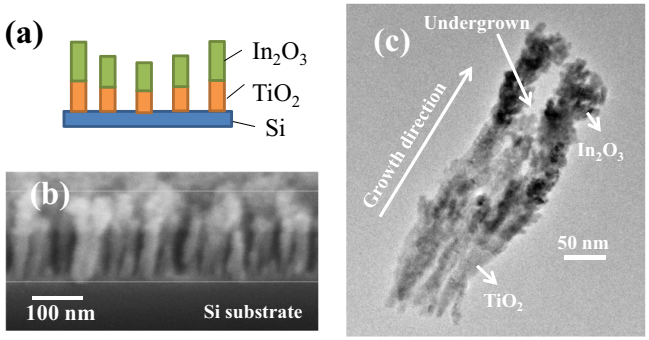

Figure 2. (**a**) Schematics of TiO_2/In_2O_3 NW, (**b**) FESEM cross section image for TiO_2/In_2O_3 NW annealed at 600 °C and (**c**) TEM image for TiO_2/In_2O_3 NW annealed at 600 °C.

The as-deposited TiO_2-In_2O_3 NWs shows two peaks representing planes (211) and (440) of cubic phase for In_2O_3 while no peak can be seen for TiO_2 due to its amorphous nature which agrees with the result reported using e-beam evaporator for deposition[21]. As annealing temperature is increased from 400 °C to 600 °C, In_2O_3 exhibited more extra peaks. Increment in the diffraction peak intensities can be observed with the increase in annealing temperature. The peak intensities increment suggest better crystallinity of the samples. There is shift in XRD spectra peak with planes (211) from samples annealed at 600 °C towards lower angle compared to samples annealed at 400 °C. This is due to lattice expansion[22]. TiO_2 in TiO_2-In_2O_3 NWs is amorphous upto 400 °C and starts to crystallize when annealed at 600 °C and exhibits anatase phase with planes (101) and (004) orientations due to its high stability[23]. Similar result was observed for TiO_2 annealed above 500 °C[24]. Moreover, the XRD peak intensities of In_2O_3 in TiO_2-In_2O_3 NWs increased with the increase in annealing temperature. As the annealing temperature is increased, crystallinity is improved. As a result, strain is reduced till 600 °C. However, for samples annealed at 800 °C, the In_2O_3 crystallinity is decreased as peak intensities is decreased compared with samples annealed at 600 °C, where the grain stops growing or exhibits amorphous nature above 600 °C as reported[14,15]. Further, TiO_2 exhibits mixed anatase-rutile phase diffraction peaks at 800 °C. Yan *et al*. also reported on the appearance of crystallization transformation from anatase to rutile phase above 600 °C[25]. Ma *et al*. reported on collapse of TiO_2 nanotube arrays structure grown at 800 °C with Ti support in oxygen owing to the mechanical stress and grain growth arising from the 'feeding effect'[26]. During the phase transformation from anatase to rutile, the TiO_2 nanowires may distort or disrupt the lattice of TiO_2. This phase transformation led to break the two Ti-O bonds in the anatase, to rearrange Ti-O in octahedral to form rutile phase[27]. Of all the annealed samples, the sample annealed at 600 °C showed better crystallinity and lesser strain. Lesser strain implies decrease in lattice imperfections[28].

Figure 2(a) shows the schematics of vertically aligned TiO_2/In_2O_3 NW array sample and Fig. 2(b) depicts the typical FESEM cross section image of the TiO_2/In_2O_3 NW sample annealed at 600 °C in which the top section is In_2O_3 and bottom being TiO_2. TiO_2 NWs is deposited beneath the In_2O_3 NW to obtain a separated TiO_2/In_2O_3 NWs because In_2O_3 has been reported to form interconnected column beyond Zone I structure even under extreme shadowing effect condition due to sufficient diffusion of surface adatoms[29]. In this zone I, the homologous growth temperature parameter ($\theta = T_S/T_m$) is less than 0.2 where T_s and T_m are the substrate temperature and melting point of the deposited material, respectively with little surface diffusion of adatoms take place and the film microstructure and texture are controlled by shadowing[30]. Figure 2a shows that NWs are aligned closely, uniformly and vertically. It can also be seen that some NWs are undergrown due to competitive growth arising from shadowing effect using the GLAD technique. The GLAD technique follows the principle of self-shadowing and vapor fluxes cancellation during azimuthal rotation of substrate to obtain perpendicular aligned growth of NW[31]. Here, with the arrival of vapor fluxes, the taller NW overshadowed the shorter neighboring NWs and as a result, the shorter NWs remain as undergrown NWs.

Figure 2(c) shows the TEM image of annealed TiO_2/In_2O_3 NW sample at 600 °C. In the junction, color contrast can be seen, which confirms the formation of TiO_2/In_2O_3 NW. From the Fig. 2(c), the NW has top and bottom diameter of ~50 nm and ~25 nm respectively. Undergrown region is also seen in the TEM image due to shadowing effect, which plays the main vital role in the formation of NWs.

Figure 3 shows the AFM images of the as-deposited and annealed (400–800 °C) TiO_2-In_2O_3 NW respectively. The images show recrystallisation due to annealing. With the increase in annealing temperature, the grains initiate to cluster and agglomerate. From the AFM analysis, root mean square (RMS) of the roughness was found to be 10.806 nm (as deposited), 3.867 nm (400 °C), 3.26 nm (600 °C) and 3.54 nm (800 °C). The decrease in the roughness with the increase in annealing temperature is due to the increase in grain size and also the grain agglomeration, which reduces the gaps between the NWs. However, at 800 °C the roughness of TiO_2-In_2O_3 NW increases. This is due to the phase transformation from anatase to rutile; the TiO_2 NWs may disrupt the lattice of TiO_2 and thus increases the roughness of the heterostructure[26,27].

The room temperature PL readings of the as-deposited and annealed samples were recorded by exciting the samples at 250 nm wavelength. Figure 4 highlights the PL emission intensity from the as-deposited and annealed TiO_2-In_2O_3 NW. From Fig. 4 it can be understood that PL intensity decreases as we increase the annealing temperature upto 600 °C and then the emission intensity decrease with further increase in annealing temperature. There is irregularity in the variation of PL intensity with annealing temperature. It has been reported that annealing treatment reduces the number of surface states[32]. On this basis, the PL intensity should shrink upon annealing.

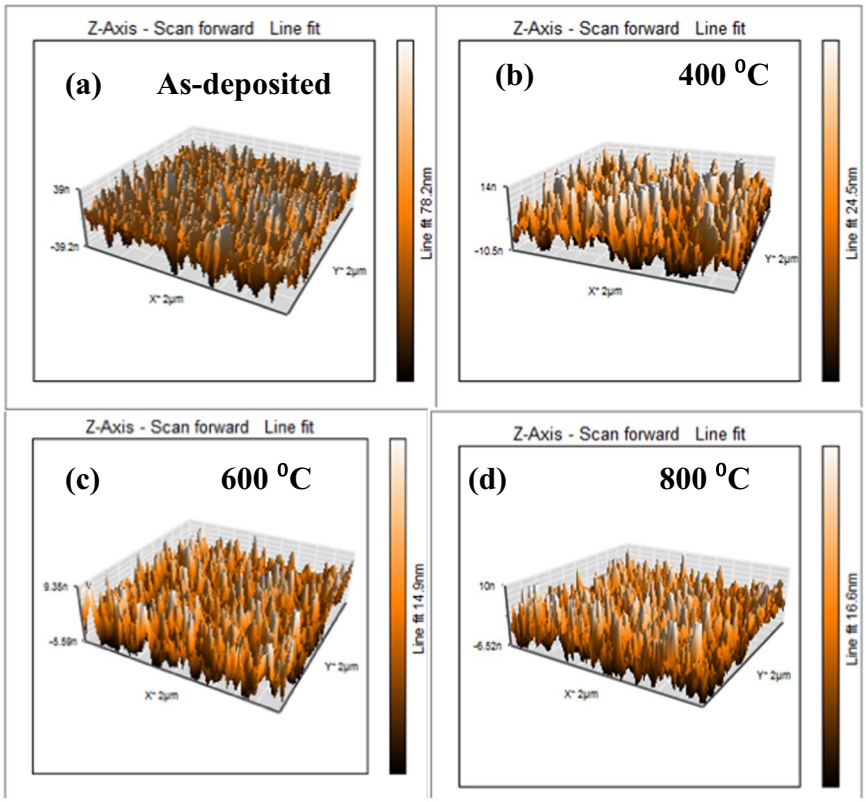

Figure 3. AFM images of TiO_2-In_2O_3 NW (**a**) as-deposited and (**b**–**d**) annealed at 400 °C-800 °C.

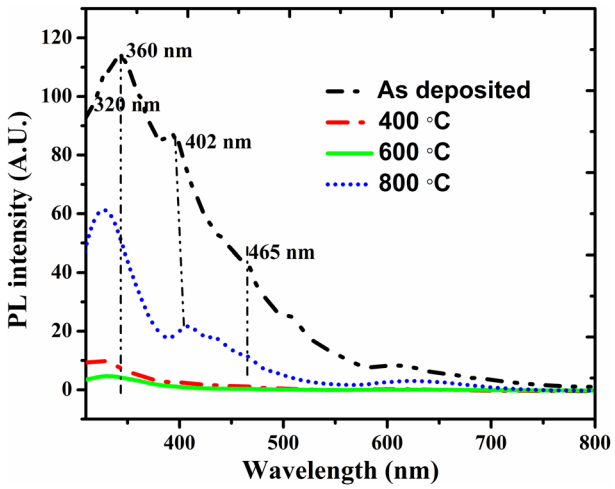

Figure 4. Photoluminescence (PL) analysis of the TiO_2-In_2O_3 NWs as-deposited and annealed samples.

However, there can be migration of defects present within the grains onto the grain surface during high temperature annealing treatment. This would raise the amount of surface states, thus enabling the PL emission to enhance to some extent. At 800 °C annealing temperature, oxygen vacancy is created in TiO_2 and may be the oxygen from In_2O_3 might diffuse into TiO_2 creating oxygen vacancy in In_2O_3. As a result, surface state is enhanced and a small shoulder PL emission is introduced at 402 nm (3.08 eV) and 465 nm (2.6 eV) related to oxygen vacancy in In_2O_3 and TiO_2 respectively in TiO_2-In_2O_3 NW samples annealed at 800 °C[33,34]. Moreover, the main-band related PL emission at 340 nm for In_2O_3 and 360 nm for TiO_2 as obtained in our previous work for TiO_2-In_2O_3 NW[35] is shifted towards shorter wavelength with increase in annealing temperature. This blue-shift cannot be related to quantum confinement[36] but can be attributed to the widening of energy bandgap with increase in the grain size, which is a function of annealing temperature. Further annealing at 800 °C, the main-bandgap PL emission should be red-shifted due to the formation of lower energy TiO_2 rutile phase, but the PL emission band is blue-shifted. This may be due to the formation of amorphous Titanium silicate where the Ti ions are diffused out toward the

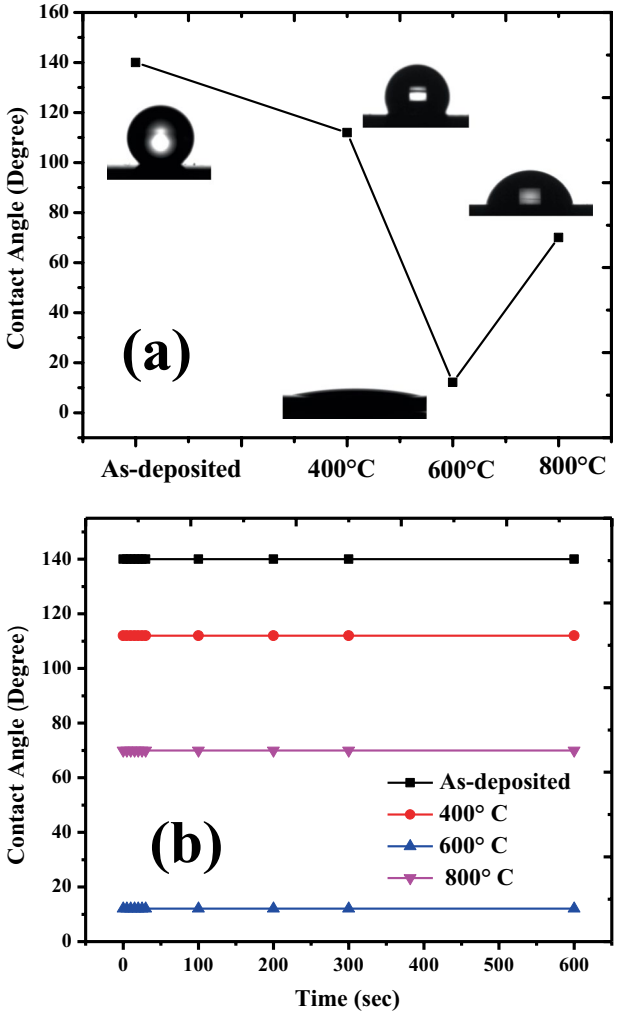

Figure 5. (**a**) Static contact angle of as-deposited TiO_2-In_2O_3 NWs and annealed samples and (**b**) Contact angle versus time plot of TiO_2/In_2O_3 NW as-deposited and annealed samples.

interface during high temperature annealing which cause the blue shift of main band gap emission[24]. It can be concluded that the grain size and annealing treatment can affect the PL emission. Taking these effects into consideration, there is possibility for PL emission to vary irregularly with the annealing treatment as shown in Fig. 4. Among the various annealed samples, samples annealed at 600 °C exhibits reduced PL emission indicating lesser defects.

Room temperature static water contact angle (θ_{WCA}) measurement was performed on the as-deposited and annealed samples. Figure 5(a) depicts the θ_{WCA} values and water dropping profile of the as-deposited and annealed samples taken during the measurement.

The as-deposited samples exhibits a higher θ_{WCA} of 140° compared to annealed samples. As reported by the author[35], as-deposited NWs structure are porous due to gap between consecutive NWs. The under-grown NWs arising due to shadowing effect creates more air gaps between the NWs and the air trapped in the gap reduces the fractional coverage at solid-liquid interface which decreases the van der waal forces at the surface. The roughness of AFM is more in as deposited samples. As a result, the θ_{WCA} value of as-deposited sample is higher due to the air trapped between TiO_2-In_2O_3 NWs. Increase in surface roughness enhances the water contact angle which is in consistent with the Cassie and Baxter[37]. Moreover, as seen from the PL analysis, the higher emission from oxygen vacancies in as-deposited TiO_2-In_2O_3 NWs might be one of the reasons for showing higher contact angle. After annealing, the samples θ_{WCA} is reduced compared to as-deposited sample and started showing nearly superhydrophilic nature. This is because after annealing the grain size of the TiO_2-In_2O_3 NWs increases, the NWs starts to cluster and agglomerate which in return reduces the air gap. Since the annealing is carried out in an ambient oxygen environment, this reduces the oxygen vacancies and the oxygen trapped by the surface and hence, θ_{WCA} reduce with the increase in annealing temperature. However, due to the change in phase of TiO_2 from anatase to rutile at 800 °C, there is lattice distortion which increases the surface roughness of heterostructure and results in trapping of more air, thus enhancing the θ_{WCA} to 70° for TiO_2-In_2O_3 NWs. It can be seen that water contact angle for all the samples is maintained when observed for 10 min as seen in Fig. 5(b).

It is also necessary to characterize the surface wetting behavior using dynamic water contact angle measurement. The advancing contact angle (θ_{ACA}) as well as receding contact angle (θ_{RCA}) are analyzed through adding

Samples	Advancing contact angle degree (θ_{ACA})	Receding contact angle degree (θ_{RCA})	Contact angle hysteresis degree (θ_H)	Sliding angle (α)	Maximum frictional force (F_{max}) (μN)	Work of adhesion (mN/m)
As-deposited	179	168	11	20	33.60399	16.54105
400 °C	153	120	33	50	75.21926	44.67327
600 °C	46.6	6	40.6	85	97.66022	142.3721
800 °C	111.3	89	22.3	60	85.00748	96.39072

Table 1. Dynamic water contact angle measurement.

and then withdrawing the liquid volume from water droplet[38]. Here, the θ_{ACA} and θ_{RCA} are the angles obtained by liquid expansion and contraction respectively and the resulting contact angle hysteresis (θ_H) are given in Table 1. The θ_H depends on the surface roughness and droplet adhesion to the surface. The value of θ_H increased with the increase in annealing temperature due to increase in interaction of surface with water droplet. The as- deposited TiO_2-In_2O_3 NW showed the least difference in the hysteresis. The hysteresis increased with the increase in annealing temperature due to decrease in θ_{WCA}. The next parameter, the sliding angle is measured. It is the angle of the droplet at which the droplet starts to slide when the substrate tilts. When the frictional force is low, the water droplet tends to slide effortlessly from the surface. The required maximum frictional force to displace liquid on surface can be found from the following Eq. (2)[39]:

$$F_{max} = mg\ sin\alpha \tag{2}$$

where m is the mass of the water, g is the acceleration due to gravity and α is the sliding angle of the droplet. Another main parameter for wetting of surface is the surface adhesion. It is the attraction of molecules between the surfaces in contact. Work of adhesion (W) between the water droplets and the surfaces of as-deposited and annealed samples are calculated respectively using young-dupre's formula as given in Eq.(3)[40].

$$W = \gamma_w(1 + cos\theta) \tag{3}$$

Where, γ_w represents the surface tension of water.

The as-deposited samples slide the water droplet when the surface was tilted at an angle of 20°. Accordingly, the force that is needed to slide the droplet of water from surface was found to be 33.60399 μN. However, the same droplet was not sliding until the tilt angle of the surface was 85° for samples annealed at 600 °C, which is due to the strong force of 97.66022 μN needed to slide the droplet from the surface. The sliding angle increased with the increase in annealing temperature because of the decrease in water contact angle. The air trapped between the nanowires is reduced due to agglomeration, grain size is increased and surface roughness is minimized. Moreover, hydrophobic surface materials acquire lower work of adhesion. The as-deposited TiO_2-In_2O_3 NW showed lower work of adhesion on comparison with annealed samples as oxygen adsorption tendency is higher at oxygen vacancy sites on the surface in as-deposited TiO_2-In_2O_3 NWs. The as-deposited TiO_2-In_2O_3 NW showed work of adhesion of 16.54105 mN/m, which increased to 142.3721 mN/m for samples annealed at 600 °C. This increase is owing to the increase in contact angle hysteresis. Tuning the oxygen vacancies and structure can change the surface roughness and hence the θ_{WCA}. The structure having higher θ_{WCA} can be used in self-cleaning surfaces whereas lower θ_{WCA} can be used in biomedical applications. The surface has been modified for tuning the surface wettability using heat treatment without any chemical surface modification which may be harmful.

Experimental detail. TiO_2/In_2O_3 coaxial NWs array is deposited on Si<100> p-type substrate inside e-beam evaporator (BC 300, HHV India) incorporating GLAD technique. Cleaned substrate cut into 1 cm × 1 cm is placed inside the e-beam chamber with base pressure and deposition rate maintained at 6×10^{-6} mbar and 0.5 $Å s^{-1}$ respectively. During deposition, the substrate holder is aligned at 85° with respect to the source and also azimuthal rotation of the substrate is maintained at rate of 20 rpm. TiO_2 NW has been deposited using GLAD technique on Si. Likewise, In_2O_3 NW was further evaporated over TiO_2 NW to obtain TiO_2/In_2O_3 NW. The film thickness was monitored by digital thickness monitor present inside the chamber. To study the annealing effect on the heterostructure NW, the as deposited samples is annealed at various temperatures ranging from 400 °C to 800 °C. Annealing has been executed using muffle furnace, maintaining the same time duration for 1 hr and 6 °C/min heating and cooling ramp rate.

The annealed TiO_2/In_2O_3 coaxial NW morphology was studied using FESEM (SUPRA 55VP, Gemini Column) and transmission electron microscope (TEM). The structural properties of the as-deposited and annealed samples were analyzed using x-ray diffraction (XRD) Cu Kα radiation (RigaKu smart lab guidance). Optical property was studied using F-7000 fluorescence spectrophotometer for photoluminescence (PL) measurement under excitation wavelength of 250 nm. Atomic force microscope (AFM) (Nanosurf, Model: Easyscan 2 AFM) was used to calculate surface roughness of the samples. Contact angle measurement was carried out using sessile drop method with contact angle meter (DMS-401, Kyowa Interface Science CO LTD, Japan).

Conclusion

Perpendicularly aligned coaxial TiO_2/In_2O_3 NW array are prepared on Si substrate using catalyst free glancing angle deposition technique within electron-beam evaporator. Wettability of TiO_2/In_2O_3 NW surface is tuned using heat treatment in which the surface properties such as phase changes, surface roughness, changes in static and dynamic contact angles are studied. The samples annealed at 600 °C shows nearly superhydrophilic with static

water contact angle of 12° and a high sliding angle of 85°. The results indicate that controlling the surface of nanostructure is essential to attain desired water contact angles and sliding angles, which is paramount for designing practical application in self-cleaning and biomedical fields.

Data availability

The datasets generated during and/or analyzed during the current study are available from the corresponding author on reasonable request.

Received: 13 March 2020; Accepted: 8 May 2020;
Published online: 10 June 2020

References

1. Chen, F. *et al*. Plasma hydrophilization of superhydrophobic surface and its aging behavior: the effect of micro/nanostructured surface. *Surface and Interface Analysis* **48**, 368–372, https://doi.org/10.1002/sia.5988 (2016).
2. Chen, F. *et al*. Stability of plasma treated superhydrophobic surfaces under different ambient conditions. *Journal of colloid and interface science* **470**, 221–228, https://doi.org/10.1016/j.jcis.2016.02.058 (2016).
3. Son, J. *et al*. A practical superhydrophilic self cleaning and antireflective surface for outdoor photovoltaic applications. *Solar Energy Materials and Solar Cells* **98**, 46–51, https://doi.org/10.1016/j.solmat.2011.10.011 (2012).
4. Belmonte, M. M. *et al*. Suitable materials for soft tissue reconstruction: *in vitro* studies of cell – triblock copolymer interactions. *J. Bioact. Compat Polym* **20**, 509–526, https://doi.org/10.1177/0883911505058608 (2005).
5. Takata, Y., Hidaka, S., Masuda, M. & Ito, T. Pool boiling on a superhydrophilic surface. *International Journal of Energy Research* **27**, 111–119, https://doi.org/10.1002/er.861 (2003).
6. Miyauchi, M., Nakajima, A., Watanabe, T. & Hashimoto, K. Photocatalysis and photoinduced hydrophilicity of various metal oxide thin films. *Chem Mater* **14**, 2812–2816, https://doi.org/10.1021/cm020076p (2002).
7. Kenanakis, G., Vernardou, D. & Katsarakis, N. Light-induced selfcleaning properties of ZnO nanowires grown at low temperatures. *Appl. Catal. A Gen* **411**, 7–14, https://doi.org/10.1016/j.apcata.2011.09.041 (2012).
8. Pooja, P., Choudhuri, B., Saranyan, V. & Chinnamuthu, P. Synthesis of coaxial TiO_2/In_2O_3 nanowire assembly using glancing angle deposition for wettability application. *Applied Nanoscience* **9**, 529–537, https://doi.org/10.1007/s13204-018-0936-0 (2019).
9. Bal, J. K., Kundu, S. & Hazra, S. Hydrophobic to hydrophilic transition of HF-treated Si surface during Langmuir–Blodgett film deposition. *Chemical Physics Letters* **500**, 90–95, https://doi.org/10.1016/j.cplett.2010.10.004 (2010).
10. Livshin, S. & Silverstein, M. S. Enhancing hydrophilicity in a hydrophobic porous emulsion-templated polyacrylate. *Journal of Polymer Science: Part A: Polymer Chemistry* **47**, 4840–4845, https://doi.org/10.1002/pola.23522 (2009).
11. Kang, E.T. & Neoh, K.G., Surface Modification of Polymers, in Encyclopedia of Polymer Science and Technology, Ed., John Wiley & Sons, New York, (2009).
12. Zhang, H. & Banfield, J. F. Phase transformation of nanocrystalline anatase-to-rutile via combined interface and surface nucleation. *J. Mater. Res.* **15**, 437–448, https://doi.org/10.1557/JMR.2000.0067 (2000).
13. Zhang, J., Li, M. J., Feng, Z. C., Chen, J. & Li, C. UV raman spectroscopic study on TiO_2. I. phase transformation at the surface and in the bulk. *J. Phys. Chem. B* **110**, 927–935, https://doi.org/10.1021/jp0552473. (2006).
14. Steffes, H., Imawan, C., Solzbacher, F. & Obermeier, E. Fabrication parameters and NO sensitivity of reactively RF-sputtered In_2O_3 thin films. *Sensors and Actuators B* **68**, 249–253, https://doi.org/10.1016/S0925-4005(00)00437-8 (2000).
15. Kraini, M., Bouguila, N., Halidou, I., Timoumi, A. & Alaya, S. Properties of In_2O_3 films obtained by thermal oxidation of sprayed In_2S_3. *Materials Science in Semiconductor Processing* **16**, 1388–1396, https://doi.org/10.1016/j.mssp.2013.04.021 (2013).
16. Wu, Y., Fan, R. & Yang, P. Block-by-block growth of single crystalline Si/SiGe superlattice nanowires. *Nano Lett* **2**, 83–86, https://doi.org/10.1021/nl0156888 (2002).
17. Guo, J. *et al*. Realizing Zinc blende GaAs/AlGaAs axial and radial heterostructure nanowires by tuning the growth temperature. *J Mater Sci Technol* **27**, 507–512, https://doi.org/10.1016/S1005-0302(11)60099-6 (2011).
18. Flynn, G., Ramasse, Q. M. & Ryan, K. M. Solvent vapor growth of axial heterostructure nanowires with multiple alternating segments of Silicon and Germanium. *Nano Lett* **16**, 374–380, https://doi.org/10.1021/acs.nanolett.5b03950 (2016).
19. Zhou, C. M. & Gall, D. Growth competition during glancing angle deposition of nanorod honeycomb arrays. *Appl. Phys. Lett.* **90**, 093103, https://doi.org/10.1063/1.2709929 (2007).
20. Cullity, B. D. Elements of X ray Diffraction, Addition, Wesley Pub, Note Dame (1978).
21. He, Y. P., Zhang, Z. Y. & Zhao, Y. P. Optical and photocatalytic properties of oblique angle deposited TiO_2 nanorod array. *J Vac Sci Technol B* **26**, 1350, https://doi.org/10.1116/1.2949111 (2008).
22. Bouhdjera, A. *et al*. Influence of annealing temperature on In_2O_3 properties grown by an ultrasonic spray CVD process. *Optik* **127**, 6329–6333, https://doi.org/10.1016/j.ijleo.2016.04.100 (2016).
23. El-Nahass, M. M., Soliman, H. S. & El-Denglawey, A. Absorption edge shift, optical conductivity, and energy loss function of nano thermal-evaporated N-type anatase TiO_2 films. *Appl. Phys. A* **122**, 775 1–10, https://doi.org/10.1007/s00339-016-0302-6 (2016).
24. Seong, N. J., Yoon, S. G. & Lee, W. J. Electrical characteristics of Ga_2O_3–TiO_2 nanomixed films grown by plasma enhanced atomic-layer deposition for gate dielectric applications. *Applied Physics Letters* **87**, 082909, https://doi.org/10.1063/1.2034100 (2005).
25. Sun, Y., Yan, K., Wang, G., Guo, W. & Ma, T. Effect of annealing temperature on the hydrogen production of TiO_2 nanotube arrays in a two-compartment photoelectrochemical cell. *J. Phys. Chem. C* **115**, 12844–12849, https://doi.org/10.1021/jp1116118 (2011).
26. Ma, Q. & Liu, S. J. Significantly enhanced structural and thermal stability of anodized anatase nanotube arrays induced by tensile strain. *Electrochemical Acta* **56**, 7596–7601, https://doi.org/10.1016/j.electacta.2011.06.081 (2011).
27. Mo, S. D. & Ching, W. Y. Electronic and optical properties of three phases of titanium dioxide: Rutile, anatase, and brookite. *Phys Rev B* **51**, 13023–13031, https://doi.org/10.1103/PhysRevB.51.13023 (1995).
28. Mathews, N. R., Morales, E. R., Corte´s-Jacome, M. A. & Antonio, J. A. T. TiO_2 thin films – Influence of annealing temperature on structural, optical and photocatalytic properties. *Solar Energy* **83**, 1499–1508, https://doi.org/10.1016/j.solener.2009.04.008 (2009).
29. Mukherjee, S. & Gall, D. Structure zone model for extreme shadowing conditions. *Thin Solid Films*. **527**, 158–163, https://doi.org/10.1016/j.tsf.2012.11.007 (2013).
30. Mondal, A. *et al*. Structural and optical properties of glancing angle deposited In_2O_3 columnar arrays and Si/In_2O_3 photodetector. *Appl. Phys. A* **115**, 353–358, https://doi.org/10.1007/s00339-013-7835-8 (2014).
31. Zhao, Y. P., Ye, D. X., Wang, G. C. & Lu, T. M. Designing Nanostructures by Glancing Angle Deposition. *SPIE Proceedings* **5219**, 59–73, https://doi.org/10.1117/12.505253 (2003).
32. Zhang, W. F., Zhang, M. S., Yin, Z. & Chen, Q. Photoluminescence in anatase titanium dioxide nanocrystals. *Appl. Phys. B* **70**, 261–265, https://doi.org/10.1007/s003400050043 (2000).
33. Zhang, F. *et al*. Fabrication of α-Fe_2O_3/In_2O_3 composite hollow microspheres: A novel hybrid photocatalyst for toluene degradation under visible light. *Journal of Colloid and Interface Science* **457**, 18–26, https://doi.org/10.1016/j.jcis.2015.06.008 (2015).

34. Huang, S., Ou, G., Cheng, J., Li, H. & Pan, W. Ultrasensitive visible light photoresponse and electrical transportation properties of nonstoichiometric indium oxide nanowire arrays by electrospinning. *J. Mater. Chem. C* **1**, 6463–6470, https://doi.org/10.1039/C3TC31051E (2013).
35. Pooja, P. & Chinnamuthu, P. Surface state controlled superior photodetection properties of isotype n-TiO_2/In_2O_3 heterostructure nanowire array with high specific detectivity. *IEEE transactions on Nanotechnology* **19**, 31–34, https://doi.org/10.1109/TNANO.2019.2956960 (2020).
36. Shougaijam, B., Swain, R., Ngangbam, C. & Lenka, T. R. Enhanced photodetection by glancing angle deposited vertically aligned TiO_2 nanowires. *IEEE Transactions on Nanotechnology* **15**, 389–394, https://doi.org/10.1109/TNANO.2016.2536162 (2016).
37. Cassie, A. B. D. & Baxter, S. Wettability of porous surfaces. *Trans Faraday Soc* **40**, 546–551, https://doi.org/10.1039/TF9444000546 (1944).
38. Drelich, J., Miller, J. D. & Good, R. J. The effect of drop (bubble) size on advancing and receding contact angles for heterogeneous and rough solid surfaces as observed with sessile-drop and captive-bubble techniques. *J Colloid Interface Sci* **179**, 37–50 (1996).
39. Guo, Z. G. *et al*. Stick and slide ferrofluidic droplets on superhydrophobic surfaces. *Appl Phys Lett* **89**, 0819 11–13, https://doi.org/10.1063/1.2336729 (2006).
40. Dupré, A. Theorie Mecanique de la Chaleur, chapter IX, Actions Moleculaires (Suite), Gauthier-Villars, Paris (1869).

Acknowledgements

The authors would like to thank and acknowledge SAIF, NEHU Shillong for TEM analysis, T.D. Singh, NIT Manipur for PL analysis and Centre of Excellence in Advanced Materials NIT Durgapur for AFM analysis, TEQIP-III and NIT Nagaland for financial assistance.

Author contributions

Pheiroijam Pooja synthesized the sample and carried out the experiment, result analysis and written the manuscript. P. Chinnamuthu, the corresponding author conceived the idea and is responsible for ensuring that the descriptions are accurate.

Competing interests

The authors declare no competing interests.

Additional information

Correspondence and requests for materials should be addressed to C.P.

Reprints and permissions information is available at www.nature.com/reprints.

Publisher's note Springer Nature remains neutral with regard to jurisdictional claims in published maps and institutional affiliations.